

**Transport of magnetic microparticles via tunable stationary magnetic traps in patterned wires**

G. Vieira,\* A. Chen, T. Henighan, J. Lucy, F. Y. Yang, and R. Sooryakumar

*Department of Physics, The Ohio State University, Columbus, Ohio 43210, USA*

(Received 8 July 2011; revised manuscript received 10 February 2012; published 30 May 2012)

Remote manipulation of fluid-borne magnetic particles on a surface is useful to probe, assemble, and sort microscale and nanoscale objects. In this paper, fields emanating from magnetic domain walls in zigzag wires as well as from magnetization distributions in notched  $\text{Co}_{0.5}\text{Fe}_{0.5}$  wires patterned on a silicon surface are shown to act as effective traps for such objects. Weak ( $\sim 100$  Oe) in- and out-of-plane external magnetic fields modify the energy landscape, allowing for the entrapped objects to be remotely maneuvered along predetermined routes across the surface while the magnetization profiles at the wire vertices and notches remain stationary. In calculating the forces, the net magnetic field and its spatial distribution are determined by modeling the wire magnetization using micromagnetic simulation or by approximating the trap as a point source of fields. The applicability of these models to particle manipulation under the experimental conditions is discussed.

DOI: [10.1103/PhysRevB.85.174440](https://doi.org/10.1103/PhysRevB.85.174440)

PACS number(s): 75.60.Ch, 87.80.Fe, 83.60.Np, 85.85.+j

**I. INTRODUCTION**

Magnetism-based manipulation, separation, and detection methods for engineering and biological applications have recently seen rapid growth in their use.<sup>1–6</sup> Among these methods, techniques that utilize superparamagnetic particles as the force-transmitting handle have been particularly promising. The nonhysteretic magnetization loops and absence of remanence or coercivity at room temperature when the particle size lies below the single domain limit ( $\sim 20$  nm for  $\text{Fe}_3\text{O}_4$ ) are attractive features of superparamagnetism that, among other attributes, render predictable forces and do not promote particle clustering in the absence of an external field.<sup>7</sup> On the other hand, the corresponding magnetic tractive force for such a tiny particle in a field gradient, which is proportional to the particle volume, is greatly diminished, requiring very large applied fields and/or high gradients to maneuver them. Although the use of macroscopic magnets in such situations is possible, they offer limited accuracy and are unpractical in many settings for manipulation of micron- and smaller-scale entities.

One approach that has emerged to generate the strongly needed inhomogeneous local fields has been via magnetic films<sup>8</sup> and patterned micromagnets<sup>9</sup> that create near-surface fields enabling fluid-borne superparamagnetic particles to be transported atop a substrate. Underlying this method are domain walls (DW) that, along with their emanating magnetic fields, are rendered mobile through the application of external fields. In these instances, the stray field-trapped particles are transported along the route defined by the trajectory of the mobile domain walls. For example, domain walls in garnet films<sup>10,11</sup> and patterned wires<sup>12–14</sup> provide fields and field gradients that are sufficiently high to trap and transport microscale magnetic particles. In addition to DW phenomena, magnetic disk,<sup>15</sup> oval,<sup>16</sup> and sawtooth<sup>17</sup> patterns have been utilized to transport magnetic particles trapped in the resulting stray field with the device magnetization and trapping locations dictated and rendered mobile by externally applied fields. In some instances, these different approaches have been extended to manipulate biological cells.<sup>18–21</sup>

In contrast to transporting particles by moving the DWs via application of external magnetic fields, we recently

demonstrated that static domain walls offer a viable means to maneuver particles and labeled cells across a surface.<sup>22</sup> In this approach, illustrated in ferromagnetic zigzag wires, weak external fields transport the targeted entities by strengthening or weakening the local fields in the vicinity of the stationary DWs at the zigzag vertices. The accompanying changes to the energy landscape across the entire platform and the corresponding attractive and repulsive directed forces offer advantages over approaches that rely on properties of mobile magnetization. These benefits include the ability to (a) maneuver and transport particles away from the ferromagnetic wire conduits (in addition to transporting particles along the wire), (b) generate the required directed forces for transport along specific surface trajectories through weak external fields ( $< 100$  Oe) produced by inexpensive miniature electromagnets, (c) weaken or strengthen the trapping potential to control Brownian fluctuations<sup>23</sup> that become more pronounced with diminishing particle size, and (d) multiplex trapping and transport of particle ensembles across a surface, thereby enabling efficient outcomes related to transfer and conveyor applications. In addition, since in this approach the DWs are stationary, they are not susceptible to pinning at topographic imperfections or defects that could hinder particle transport.

In this paper, we present results associated with stationary magnetization in microscopic magnetic wires of a rectangular cross-section patterned on a surface to trap and transport miniature ( $< 10$   $\mu\text{m}$ ) magnetic particles along programmed routes. Two types of engineered surfaces are discussed for the purpose of creating traps. First, we investigate a previously established technique of using stationary domain walls in patterned zigzag wires with regular turns (vertices) for trapping particles.<sup>22–24</sup> Second, a new particle trapping technique, based on straight wires with periodic indentations (notches), is studied. In particular, by selecting a high-shape anisotropy design for the notched or zigzag wire and a particular ferromagnetic material ( $\text{Co}_{0.5}\text{Fe}_{0.5}$ ), our investigation focuses on conditions where the wire magnetization is substantially unchanged and the DW does not leave the immediate vicinity of the trapping site for low ( $< 100$  Oe) external magnetic fields. The DW magnetization profiles at the wire vertices and notches are

evaluated via micromagnetic simulation, magneto-optical Kerr effect (MOKE) microscopy, and magnetic force microscopy (MFM). For the low external fields ( $\sim 100$  Oe), the highly compact, large field gradients ( $>10^4$  T/m) and associated forces arising from the stationary DW enable individual fluid-borne magnetic particles in the 10-nm to 10- $\mu\text{m}$  range to be steered across the platform in a controlled manner. In calculating the forces from the two distinct wire patterns, the net magnetic field and its spatial distribution are determined either as resulting from the micromagnetic magnetization distribution of the wire or by approximating the domain wall/notch as a point charge/point dipole. We consider the applicability of these models to particle manipulation under the experimental conditions reported in this paper.

## II. EXPERIMENTAL METHODS

The zigzag and notched wires, made of  $\text{Co}_{0.5}\text{Fe}_{0.5}$ , are patterned on a silicon wafer with natural oxide by initially spin coating and then baking two layers of e-beam resist (methyl methacrylate and polymethyl methacrylate) onto the  $\text{Si}/\text{SiO}_2$  wafer. A scanning electron microscope (FEI, Hillsboro, OR) was used to pattern the desired wire geometries prior to magnetron sputtering a 40-nm-thick layer of  $\text{Co}_{0.5}\text{Fe}_{0.5}$ . Warm acetone enabled subsequent liftoff of the e-beam resist, and a 20-nm Au capping layer with a 1-nm permalloy seed layer was sputtered atop the entire substrate. A momentary in-plane magnetic field (5 kOe) was applied to orient the magnetization vectors in the zigzag wires to generate domain walls at the wire turns.<sup>25</sup> Similarly, an in-plane field (5 kOe) applied along the length of the straight wires oriented the magnetization in the notched wire. The wire-based platforms were then placed in the setup illustrated in Fig. 1 to track the trajectories of fluid-borne magnetic particles under the influence of fields created by the  $\text{Co}_{0.5}\text{Fe}_{0.5}$  wires and weak external magnetic fields. The in-plane applied fields ( $H_x$ ,  $H_y$ ) are generated

by four small electromagnets while the out-of-plane ( $H_z$ ) field is derived from a coil. Fields  $H_x$ ,  $H_y$  ( $<150$  Oe) are produced by connecting each electromagnet to independent current channels programmed in LabView software (National Instruments, Austin, TX); the direction of  $H_z$  was also reversed through programmed routines. The particles utilized in this study consist of small ( $\sim 10$  nm) iron oxide nanoparticles embedded in a polymer matrix with radius  $R = 2.3$  or 1.4  $\mu\text{m}$  (SPHERO CM-40-10, Spherotech, Lake Forest, IL, and Dynabead M280, Invitrogen, Carlsbad, CA). To avoid adhesion of the microparticles to the surface, they were placed in a solution of 0.05% Triton X-100 (Dow, Midland, MI, USA). A key feature of the spheres is their superparamagnetic character that enables them to be readily magnetized in fields of only a few tens of Oersted at room temperature and display no remnant magnetization after removal of the field.

The magnetic domains along the wires were observed through use of a commercial magnetic force microscope (MFM) and a magneto-optic Kerr effect (MOKE) setup built in our laboratory. A brief description of the MOKE system (with schematic illustrated in Fig. 8) and our procedure for acquiring images are provided in Appendix A.

## III. MICROMAGNETIC SIMULATION

To model the magnetic forces on a superparamagnetic particle, we considered the magnetization profiles at the vertices (zigzag wire) and notches (straight wire). Computer simulations based on the 2D version of the Object-Oriented Micromagnetic Framework (OOMMF) program yielded the micromagnetic structure associated with the wires.<sup>26</sup> Vectorial maps of these magnetic configurations were generated using a cell size of 20 nm over the  $\text{Co}_{0.5}\text{Fe}_{0.5}$  domain wall (saturation magnetization 2 T, exchange constant  $1.5 \times 10^{-11}$  J/m, no crystalline anisotropy). An initial, spatially uniform magnetization along the  $+y$  or  $+x$  direction (for 40-nm-thick, 1- $\mu\text{m}$ -wide zigzag or notch wires, respectively) was allowed to relax to yield equilibrium magnetization configurations. The resulting vector data provides the spatially dependent magnetization  $\mathbf{M}(x,y,z)$  with the magnetization remaining largely in plane for the modest out-of-plane fields ( $H_z < 150$  Oe) used in this study.

## IV. RESULTS: MAGNETIZATION PROFILES, ENERGY CONTOURS, AND PARTICLE TRANSPORT

### A. Zigzag wires

Figure 2(a) shows results of the micromagnetic simulation of the equilibrium domain wall structure at the vertex for a 1- $\mu\text{m}$ -wide, 40-nm-thick zigzag wire. The magnetization in the wire arms is found to transition from pointing up right to pointing up left. Because of the relatively large width of the wire, the domain wall cannot be classified as purely transverse or vortex type, but instead consists of multiple transition regions. Figure 2(b) shows a magnetic force microscope (MFM) image of light and dark spots at alternating vertices that correspond to head-to-head (HH) and tail-to-tail (TT) domain walls, respectively. Figure 2(c) illustrates a magneto-optical image where the different magnetization orientations within alternate zigzag arms lead to the interchanging bright and

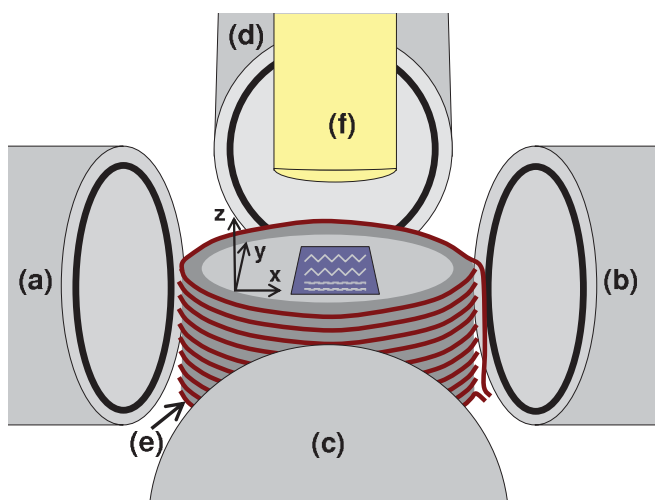


FIG. 1. (Color online) Electromagnet and microscope configuration used to manipulate and image magnetic particles on patterned magnetic structures. The setup consists of electromagnets that produce in-plane magnetic field components (a) and (b)  $H_x$  and (c) and (d)  $H_y$ , (e) a coil that produces the out-of-plane field  $H_z$ , and (f) a microscope objective.

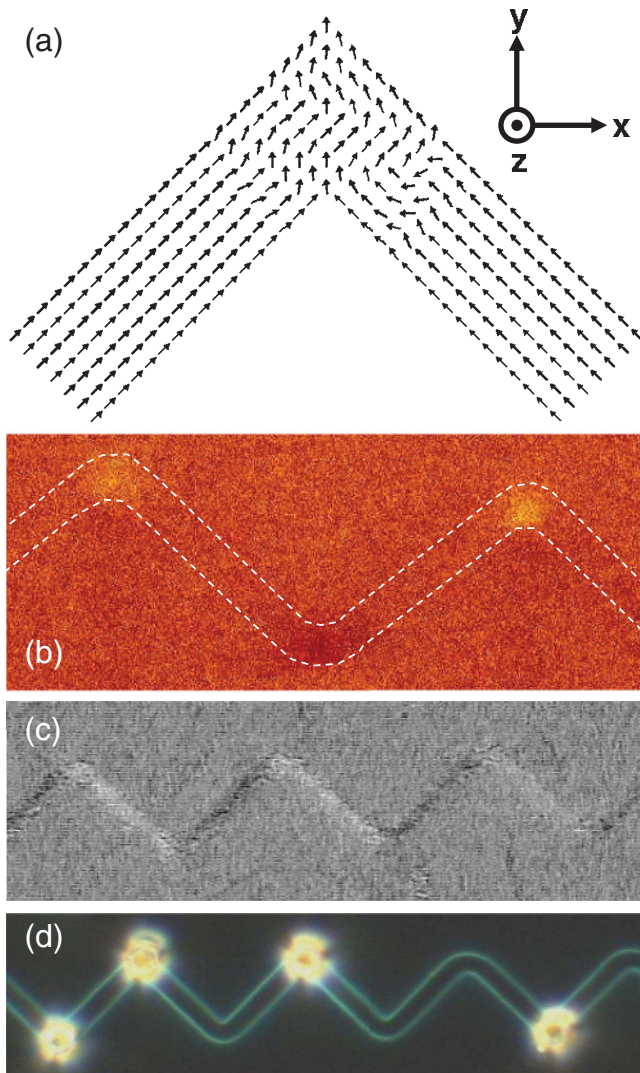


FIG. 2. (Color online) (a) Magnetic configuration of a head-to-head (*HH*) domain wall in a 1- $\mu\text{m}$ -wide, 40-nm-thick zigzag  $\text{Co}_{0.5}\text{Fe}_{0.5}$  wire as derived from micromagnetic OOMMF simulation, after relaxation from a uniform  $+y$  initial magnetization. (b) A magnetic force microscopy image of a  $\text{Co}_{0.5}\text{Fe}_{0.5}$  zigzag wire showing alternating bright and dark *HH* and tail-to-tail (*TT*) domain walls at vertices. (c) A grayscale MOKE image. Bright and dark contrast shows the alternating magnetization component ( $M_x$ ) of adjacent arms in zigzag wire. (d) A dark field image of  $\text{Co}_{0.5}\text{Fe}_{0.5}$  zigzag wire showing 2.8- $\mu\text{m}$  magnetic particles trapped at vertices. Vertex-to-vertex separation is 16  $\mu\text{m}$  in all images.

dark MOKE signals for the  $M_x$  magnetization component. Figure 2(d) shows a dark field image of 2.8- $\mu\text{m}$  diameter magnetic spheres trapped at domain walls at the vertices of the  $\text{Co}_{0.5}\text{Fe}_{0.5}$  wires.

Note that, for  $\text{Co}_{0.5}\text{Fe}_{0.5}$  wires, a magnetic field of 5 kOe was used in the MOKE system to attain oppositely magnetized images for image subtraction (see Appendix A). However, when significantly weaker fields, up to a few hundred Oe, were used, the MOKE image contrasts would not appear. This feature indicates that a few hundred Oe fields are too weak to remagnetize the  $\text{Co}_{0.5}\text{Fe}_{0.5}$  wires in this geometry. The lack of such a MOKE contrast suggests that for our

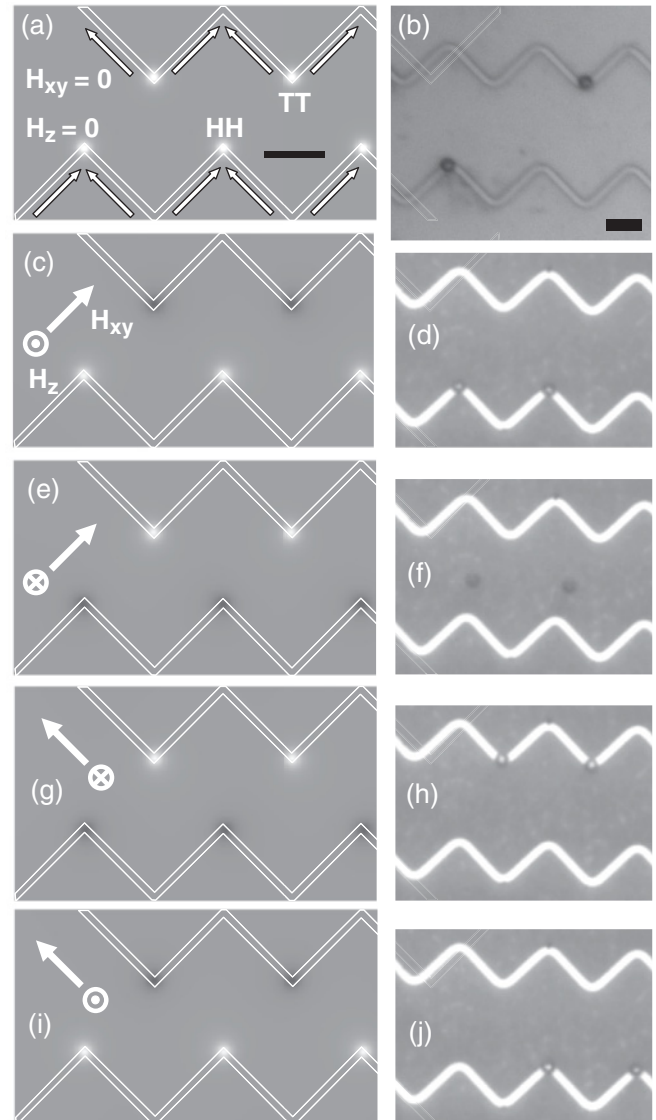


FIG. 3. Left column: Calculated potential energy landscapes of zigzag wire, where brighter shades in grayscale background image indicate lower potential energy (i.e. trap). Right column: Images of 2.8- $\mu\text{m}$ -diameter magnetic particles trapped at corresponding vertices and subsequently maneuvered in response to changing fields  $H_{xy}$  and  $H_z$ . (a) and (b) In the absence of an external field, both *HH* and *TT* domain walls are traps for the superparamagnetic particles. The scale bars represent 10 microns. (c) The combination of  $H_z = 120$  Oe and  $H_{xy} = 25$  Oe fields render some vertices to remain as traps while others transform to repulsive sites. (d), (f), (h), and (j) Two magnetic particles manipulated from one wire to the next and back based on the magnetic field sequence indicated by white arrows in (c), (e), (g), and (i), respectively. Inverting the magnetic field sequence reverses the direction of particle transport. Energy minima associated with secondary traps, only present under external fields, are too weak to be evident in the grayscale energy landscapes.

experimental conditions (external fields  $\leq 150$  Oe), the wire magnetization would remain substantially unchanged during particle transport. In contrast, for similar wire-based devices made of permalloy, fields on the order of a few hundreds of Oe were sufficient to significantly remagnetize the wires.<sup>9</sup>

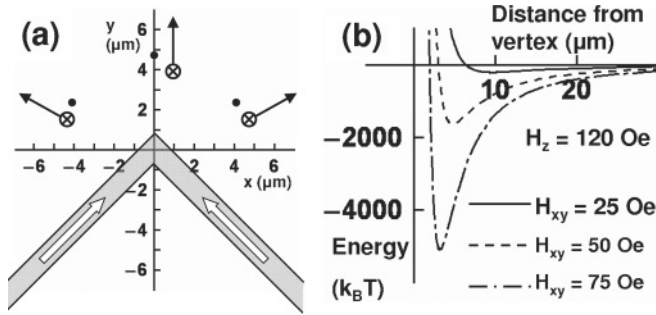


FIG. 4. Characteristics of secondary potential energy minima. (a) Schematic of locations of secondary minima, indicated by black dots, for a particle near an  $HH$  domain wall in the presence of  $H_{xy} = 50$  Oe and  $H_z = 120$  Oe. Each dot corresponds to the calculated potential minimum for field directions defined by the nearest black arrows, indicating that the direction of  $H_{xy}$  dictates the particle trajectory. (b) Potential energy landscapes for  $H_z = 120$  Oe and various  $H_{xy}$  values showing that the depth and width of secondary traps is tunable by changing the magnitude of  $H_{xy}$ .

As discussed in Appendix B, the magnetic fields, gradients, and forces associated with the wires can be calculated either by assuming a point charge at the wire vertex or by modeling the discretized magnetization of the wire. Figure 3 presents the calculated grayscale potential energy landscapes (left column) associated with a  $2.8 \mu\text{m}$ -diameter microparticle in the presence of this  $\text{Co}_{0.5}\text{Fe}_{0.5}$  wire, as well as images related to corresponding experimental particle manipulation (right column). The calculated potential energy landscapes are based on point charge approximations of the vertices. Figure 3(a) shows calculated potential energy landscapes of the trapping platform with the brighter shade representing lower energy. As indicated [Fig. 3(a)], in the absence of an external field, low energy sites (i.e. traps) arise at both  $HH$  and  $TT$  domain walls [Fig. 3(b)] for superparamagnetic microparticles.

Application of an external field  $H_z = 120$  Oe directed perpendicular to the platform plane creates repulsive centers (dark spots) at alternating vertices evident in Figs. 3(c), 3(e), 3(g), and 3(i). An in-plane field  $H_x, H_y$  creates a secondary trap away from the wire, displaced a few microns from these repulsive centers, where the line connecting the vertex (domain wall) and this secondary trap is parallel to the direction of the net in-plane field  $\mathbf{H}_{xy} = H_x\hat{x} + H_y\hat{y}$ . Note that due to the shallowness of the secondary traps, they are not directly visible in the grayscale energy landscape plots of Fig. 3. The occurrence of the secondary trap and its response to external fields are however more clearly illustrated in Fig. 4. The location of the secondary trap thus specifies the direction in which the particle is steered from the vertex [Fig. 4(a),  $H_{xy} = 50$  Oe (black arrows) and  $H_z = 120$  Oe (circles with enclosed Xs)]. In the absence of an in-plane applied field, the secondary minimum does not exist. The characteristics of the trap (depth, width, and location) are tunable by the external in-plane field. For example, using the point charge model discussed below, Fig. 4(b) illustrates the secondary trap for  $H_z = 120$  Oe and  $H_{xy} = 25$  Oe, 50 Oe, and 75 Oe, that respectively lead to increasing trap depth and decreasing trap width. This correlation between field strength and trap features is consistent with observed particle manipulation results. For

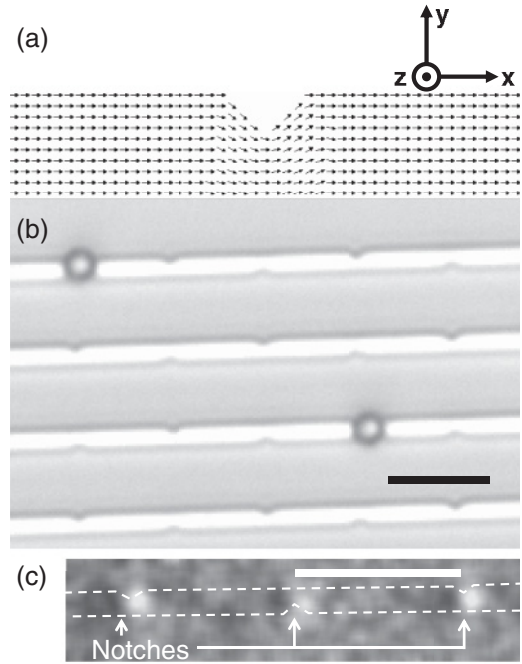


FIG. 5. (a) Magnetization configuration in a notched straight  $\text{Co}_{0.5}\text{Fe}_{0.5}$  wire as derived from micromagnetic simulation, after relaxation from a momentary uniform  $+x$  initial magnetization. (b) A bright field image of  $\text{Co}_{0.5}\text{Fe}_{0.5}$  wires showing  $2.8\text{-}\mu\text{m}$  magnetic particles trapped at notches. (c) Magnetic force microscope image of a notched  $\text{Co}_{0.5}\text{Fe}_{0.5}$  straight wire shows dark/light spots to left/right of each notch. The MFM image has been blurred using a standard Gaussian blurring technique. Scale bars in (b) and (c):  $10 \mu\text{m}$ .

instance, for manipulation over long distances ( $>10$  micron) shown in Fig. 3, a weak, in-plane field  $H_{xy} = 25$  Oe was used to weaken the deep confining potential ( $\Delta U \gg k_B T$ ) and ensure that the particle could be maneuvered along the platform plane to an adjacent vertex.

In Fig. 3(c) ( $H_z = 120$  Oe and  $H_{xy} = 25$  Oe), the point charge model reveals traps at  $HH$  walls (white spots) and repulsive sites at  $TT$  domain walls (dark spots). Correspondingly, magnetic particles are trapped only at  $HH$  domain walls [Fig. 3(d)]. Upon reversing  $H_z$ , the  $HH$  domain walls become repulsive [Fig. 3(e)], and the trapped particles are steered to secondary traps upward and to the right of the vertices [Fig. 3(f)] to be captured by the  $TT$  domain wall [Fig. 3(h)]. Reorienting  $H_x, H_y$  [Fig. 3(g)] redirects the particles in preparation for transport to a new set of vertices. Once again, reversing the direction of  $H_z$  switches traps and repulsive centers [Fig. 3(i)], and the particles are transported down and to the right to be trapped at  $HH$  domain walls [Fig. 3(j)]. The general rightward trajectory of particle movement is dictated by the sequence in which the external fields are applied. Inverting the sequence reverses the particle trajectory (see videos 1 and 2 in the supplementary material,<sup>27</sup> which illustrate such one- and two-particle manipulation, including the momentary localization of particles at secondary traps, as discussed above).

## B. Notched wires

Straight wires with periodic notches patterned along its length on alternate edges were investigated. Results of the

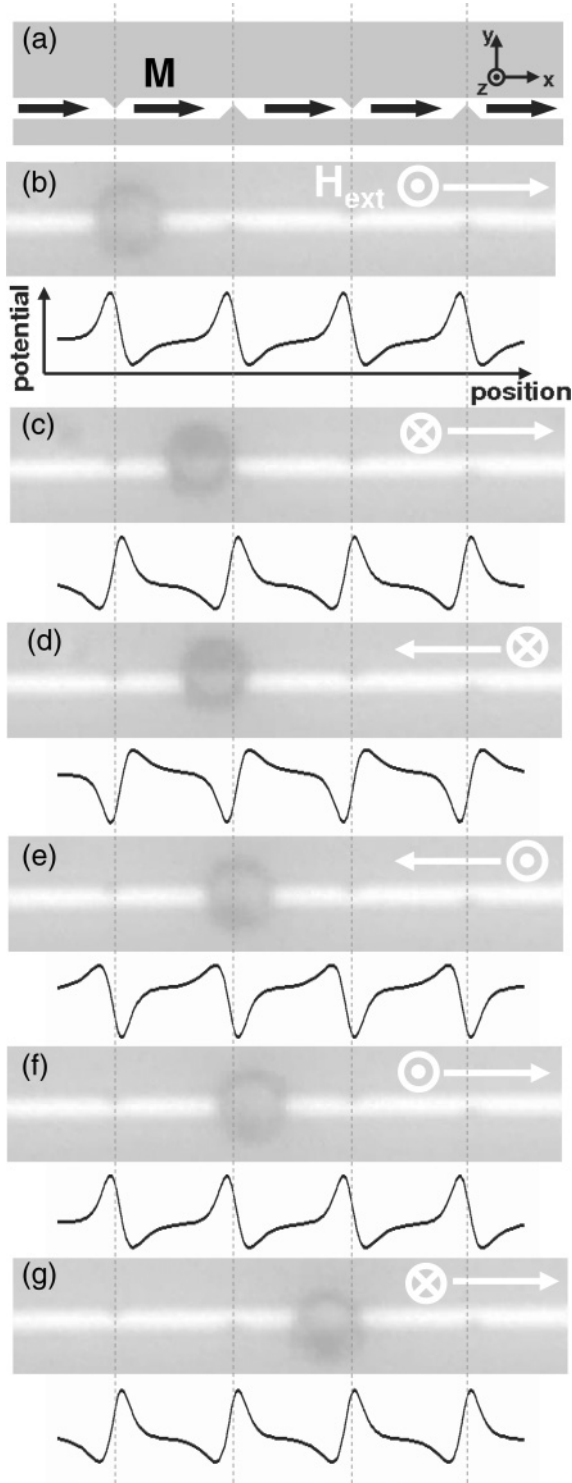


FIG. 6. (a) Schematic of magnetization configuration of a notched wire. (b)–(g) A  $4.5\text{-}\mu\text{m}$ -diameter magnetic particle transported from left to right by sequencing the out-of-plane ( $H_z$ ) and in-plane ( $H_{xy}$ ) external magnetic fields as indicated by white arrows on right. Paired under each image is the calculated magnetic energy landscape along the wire. Particle positions correlate well with local energy minima. Reversing sequence of magnetic fields reverses the direction of particle motion. Notch-to-notch distance is  $10\ \mu\text{m}$  in all images.

corresponding OOMMF simulation applied to  $1\text{-}\mu\text{m}$ -wide,  $40\text{-nm}$ -thick straight  $\text{Co}_{0.5}\text{Fe}_{0.5}$  wires with a single notch on

one edge that extends inward by a length equal to one third of the width are shown in Fig. 5(a). Similar to the case of zigzag wires, the straight wire was momentarily magnetized by a  $5\text{-kOe}$  field, however, in this instance in the  $+x$  direction, resulting in a mostly uniform magnetization along the length of the straight wire [Fig. 6(a)]. The magnetization realigns at the notch to contour with the wire edge, creating regions of changing magnetization, which coincide with locations of particle traps. Figure 5(b) shows two  $2.8\text{-}\mu\text{m}$ -diameter magnetic particles trapped at notches in straight  $\text{Co}_{0.5}\text{Fe}_{0.5}$  wires. Magnetic force microscopy imaging [Fig. 5(c)] shows dark/light spots to the left/right of each notch, indicating that the magnetic configuration in the immediate vicinity of the notch is consistent with approximating each notch as a magnetic dipole (see Appendix B), which gives the repulsive/attractive energy contour in Fig. 6.

In the absence of external fields, a particle is trapped in the vicinity of a notch. Under the application of  $\sim 100\text{-Oe}$  fields, trapping locations can be moved (despite the magnetization profile remaining substantially unchanged). Figure 6 shows a  $4.5\text{-}\mu\text{m}$ -diameter particle tracking the location of the calculated local potential minima for the prescribed external field orientation when it is steered from left to right along the wire by sequencing the external fields. As evident in video 3 of the supplementary material,<sup>27</sup> when the order of field applications is reversed, the particle is transported to the left.

## V. FORCE CALCULATIONS

The magnetization of superparamagnetic particles increases linearly for low fields and asymptotically approaches a saturation magnetization at high fields, as is schematically illustrated in Fig. 7(a). For the  $\text{Fe}_3\text{O}_4$  nanoparticles that make up the magnetic microspheres used in this study, saturation occurs at fields greater than a few kOe, and the range of external fields used in this study ( $\leq 150\ \text{Oe}$ ) is contained within the linear region near the origin of Fig. 7(a).<sup>28</sup> In this linear response region, the magnetic moment  $\mathbf{m}$  of a superparamagnetic particle can be approximated by  $\mathbf{m} = \chi_m V \mathbf{H}$  where  $\chi_m$  and  $V$  are the particle susceptibility and volume, respectively. The equation for a force on a generic paramagnetic object  $\mathbf{F} = \mu_0(\mathbf{m} \cdot \nabla)\mathbf{H}$  yields a force  $\mathbf{F} = \frac{1}{2}\mu_0\chi_m V \nabla H^2$  (Ref. 18) far from saturation, where  $\mu_0$  is the magnetic permeability in free space. The corresponding energy  $U = -\frac{1}{2}\mu_0\chi_m V H^2$  shows that the energy minimum occurs at locations of highest field magnitude  $H$ . This is generally true as long as  $M$  increases monotonically with  $H$ .

We estimate the fields arising from a given domain wall configuration using approaches based on (i) effective point charges/dipoles, (ii) dipole distributions, and (iii) magnetic charge distributions, as discussed in Appendix B. The corresponding fields, field gradients, and forces are calculated at the particle center [Figs. 7(b)–7(g)] utilizing the OOMMF-derived equilibrium magnetization configuration.

Figures 7(b) and 7(c) illustrate the calculated magnetic field as a function of height  $z$  directly above the center of a vertex or notch. The thick, dotted, and thin lines, respectively, representing the point charge/dipole, dipole distribution, and

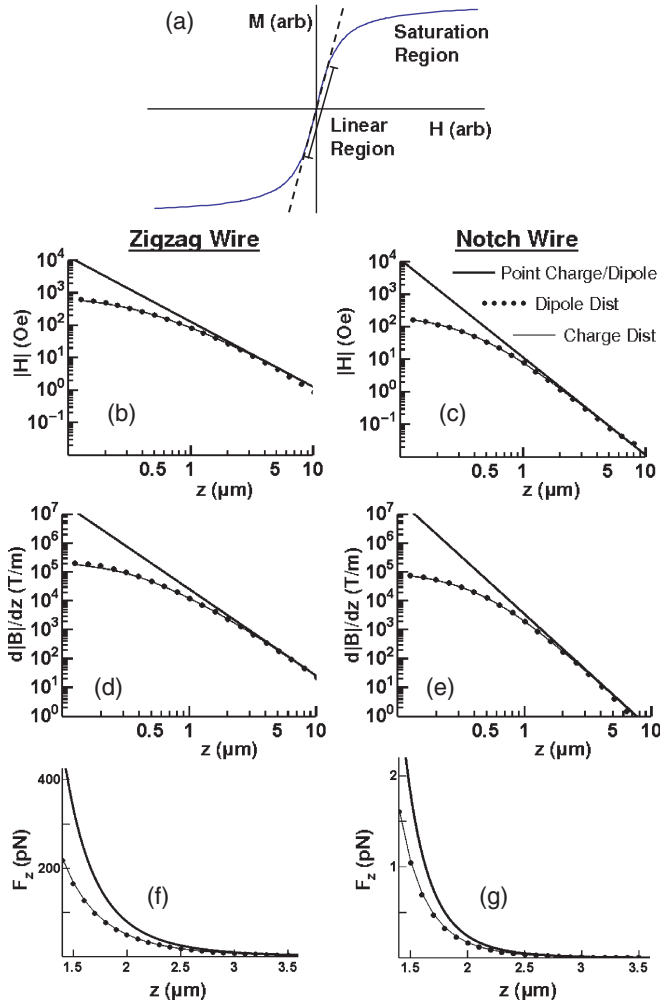


FIG. 7. (Color online) (a) Cartoon plot illustrating magnetization ( $M$ ) versus applied field ( $H$ ) for a superparamagnetic particle. At low fields,  $M$  varies approximately linearly with  $H$ , while at high fields,  $M$  saturates asymptotically. (b) and (c) Magnetic fields and (d) and (e) field gradients as a function of height  $z$  directly above a domain wall in a zigzag or notch wire. Calculations based on the point charge/dipole, dipole distribution, and charge distribution models reveal localized fields ( $>100$  Oe) and large gradients ( $>10^4$  T/m) in the immediate vicinity of the traps. (f) and (g) Calculated forces as a function of  $z$  on a  $2.8\text{-}\mu\text{m}$ -diameter magnetic particle with susceptibility  $\chi = 0.85$  for zigzag and notch wire traps.

charge distribution models, as described in the appendix, yield similar results for heights in the range  $\sim 2\ \mu\text{m} \leq z \leq \sim 10\ \mu\text{m}$ . As noted in the appendix, the point source models do not take into account the specific microscopic magnetization configuration, but rather approximate the profile by a monopole-like point charge  $q_m$  or a point dipole  $\mathbf{m}_d$ . This approximation accounts for the deviations evident for  $z < 2\ \mu\text{m}$  in the point-source-derived field values from those based on the more realistic dipole- and charge- distribution models.

In comparing near-source ( $z < 500$  nm) magnetic fields from domain wall (zigzag) traps and notch traps, they are calculated to be within an order of magnitude of each other. However, as dipole fields, the notch field falls off significantly faster ( $\sim 1/r^3$ ) than the domain wall fields ( $1/r^2$ ). The

corresponding field gradients ( $d|\mathbf{B}|/dz$ ) above the vertex/notch are illustrated in Figs. 7(d) and 7(e). Field gradients from domain wall (zigzag) traps are found to rise well above  $10^4$  T/m for  $z < 1000$  nm. This is an important characteristic for trapping and manipulating low volume magnetic particles ( $<100$  nm in diameter), which are susceptible to fluid drag forces and Brownian motion.<sup>24</sup> Figures 7(f) and 7(g) show the vertical component of the force ( $F_z$ ) on a  $2.8\text{-}\mu\text{m}$ -diameter particle ( $\chi_m = 0.85$ ) as a function of height  $z$  above the vertex/notch. The plot shows that, when localized at the domain wall ( $z = 1.4\ \mu\text{m}$ ), the trapping force is several hundred picoNewton (pN), while the forces associated with notch traps are significantly lower at a few pN. As comparison, a stationary  $2.8\text{-}\mu\text{m}$ -diameter particle in  $100\text{-}\mu\text{m/s}$  fluid flow experiences a drag force of about 2 pN, while a DNA molecule, tethered to a magnetic particle and fully extended by magnetic tweezers, results in a recoil force that ranges between 0–20 pN.<sup>29</sup>

Finally, we note that the robustness of this experimental ferromagnetic wire-based manipulation scheme will depend on the stability of the magnetic properties of the fabricated wires. For example, oxidation of the metal or repeated use of the platform could lead to changes in the magnetic characteristics of the wire. In particular, if the saturation magnetization were modified by a multiplicative factor  $\mu$ , then while the field and field gradient would be altered by the same factor, the magnetic force would change by a factor  $\mu^2$  of the original value. Thus, a 10% degradation in  $M_s$ , for example, would lead to a more substantial 19% reduction in the trapping force  $F_z$ . Experiments based on observing particle trapping in the presence of controlled fluid flow, tracking particle fluctuations while at trapping locations, and stretching DNA with well-known force extension curves (now a metrology standard<sup>30</sup>) while in the vicinity of traps could be used to verify the calculated forces.

## VI. CONCLUSION

We have demonstrated a technique for trapping magnetic particles at microscopic vertices and notches in patterned wires with the ability to remotely manipulate them through weak external magnetic fields. Unlike many other approaches where the particle transport is restricted to conduits along which the DW motion occurs, in the present study, the magnetic domain walls and profiles associated with the wires remain stationary as the particles are maneuvered across the platform along trajectories that are not restricted to the wires. The models described in this paper provide qualitative explanations of some of the more subtle characteristics, such as the ability to (i) steer particles with weak external fields ( $<100$  Oe) away from the wires or along them in predetermined directions, (ii) localize the fluid-borne particles within a trap for extended time periods (tens of minutes), and (iii) provide rapid particle transit times that are limited only by protocols that modulate the external fields and the fluid environment.

While the magnetic fields and their gradients emanating from the miniature surface profiles play a central role in steering the particles across a surface, use of standard optical or e-beam lithography methods allow for large numbers of traps

to be fabricated on a single device. Furthermore, since the weak external magnetic fields necessary for manipulation generally do not interfere with chemical or biological interactions, this approach has the potential for wide ranging applications. These features thus lend themselves to be integrated into microfluidic devices for biological cell<sup>9,21,22</sup> and microparticle sorters, as well as next-generation biomedical devices. For instance, we envision scale up for transporting  $\sim 10^6$  magnetic particles on a single centimeter-sized platform. Moreover, by conjugating magnetic particles to a biological cell, these tethered entities could be steered to a location-specific stimulus for eventual interrogation. The potential for large-scale multiplex operation would also lend this an attractive approach for rapid sequential analysis operations that do not rely on ensemble averaging.

### ACKNOWLEDGMENTS

This material is based upon work supported by the US Army Research Office under Contract No. W911NF-10-1-0353 and the Ohio State University Institute for Materials Research.

### APPENDIX A: MOKE SETUP

To obtain the MOKE signal from, for example, the  $M_x$  component of the in-plane magnetization  $\mathbf{M} = M_x \hat{x} + M_y \hat{y}$ ,  $y$ -polarized white light is incident through half of the rear aperture of an objective lens whose central axis is along  $\hat{z}$  so that  $p$ -polarized light is obliquely incident on the wire surface (i.e.  $yz$  plane of incidence; see Fig. 8 for a schematic of the MOKE setup). The resulting  $p$ -polarized component of the reflected light increases or decreases (depending on the direction of  $M_x$ ) by an amount proportional to  $M_x$  due to the

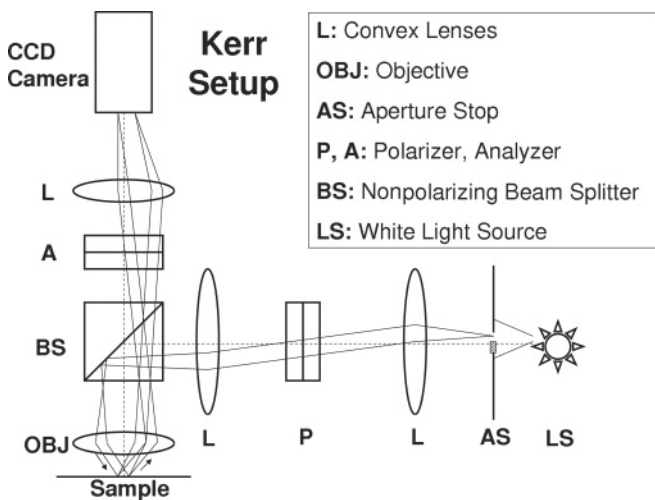


FIG. 8. Schematic of the magneto-optical Kerr effect (MOKE) setup for imaging magnetic domains. Polarized white light is incident through half of the rear aperture of an objective lens so that light is obliquely incident on the surface of interest. The resulting polarized component of reflected light increases or decreases by an amount proportional to the sample magnetization. The analyzer transmits only the desired polarization of reflected light to the CCD camera, and the MOKE signal is processed digitally. The result is a grayscale image which coincides with sample magnetization.

transverse MOKE. The analyzer placed before a CCD camera transmits only  $p$ -polarized reflected light. The image recorded when the medium is magnetized in one direction is subtracted digitally from that recorded with the magnetization in the opposite direction and the resulting spectrum amplified 100-fold. The result is a grayscale image where white-gray-black corresponds to an  $M_x$  value that is positive-zero-negative. A similar approach can be implemented to monitor the  $M_y$  component.<sup>31</sup> See Fig. 8 for a schematic of the MOKE setup.

### APPENDIX B: FIELD CALCULATION METHODS

#### 1. Point charge/dipole model for field calculation

This model describes magnetic fields as arising from a point source, either an effective point charge  $q_m$  (i.e. monopole-like) or a point dipole. An effective point charge is given by  $q_m = -\int_S \mathbf{M}(x, y, z) \cdot \hat{n} dA$  where  $\mathbf{M}(x, y, z)$  is the spatially dependent magnetization of the wire,  $\hat{n}$  an outwardly directed normal to the surface. In the case of a domain wall,  $q_m = 2M_s w t$ , where  $M_s$ ,  $w$ , and  $t$  are, respectively, the saturation magnetization, width, and thickness of the wire. The magnetic field at location  $\mathbf{r}$  from this effective charge at the origin is

$$\mathbf{H}(\mathbf{r}) = \frac{q_m \mathbf{r}}{4\pi r^3}. \quad (\text{A1})$$

In the case of the notches, the total effective charge is zero, and the notch can be approximated as a point dipole. The magnetic field at a distance  $\mathbf{r}$  from a dipole moment  $\mathbf{m}_d$  is given by

$$\mathbf{H}(\mathbf{r}) = \frac{1}{4\pi r^3} [3(\mathbf{m}_d \cdot \hat{r})\hat{r} - \mathbf{m}_d]. \quad (\text{A2})$$

While the point charge ( $q_m$ ) was calculated based on geometric considerations, the point dipole  $\mathbf{m}_d$  associated with the notch traps was calculated to be  $1.2 \times 10^{-14} \text{ Am}^2$  by fitting the fields from the point dipole model at large  $z$  ( $> 2 \mu\text{m}$ ) to those derived from dipole and charge distribution models. In comparison, a typical superparamagnetic bead 1 micron in diameter in a 100-Oe magnetic field has a magnetic moment of  $10^{-15} \text{ Am}^2$ .

Either point source model works best for  $r \gg w$  (wire width). Closer to the domain wall or notch, the precise magnetization profile is needed for a more realistic calculation of the magnetic field in the immediate vicinity of the wire. The following approaches provide a better description of the field profile close to the trap.

#### 2. Dipole and charge distribution model for field calculation

The OOMMF simulations yield the magnetization profile as a 2D grid of magnetized cells. A cell located at  $(x, y, z)$  is characterized by a magnetic dipole of moment  $\mathbf{m}_d(x, y, z) = \mathbf{M}(x, y, z)V_C$ , where  $V_C$  is the volume of the cells. While each dipole can, in general, orient in any direction in three dimensions, in the present case, the magnetization is primarily confined to the  $xy$  plane of the ultra-thin, 40-nm-thick wire. Summing the fields originating from all of the dipoles [Eq. (A2)] provides the resulting magnetic field and its spatial distribution.

The magnetic field from the domain wall can also be determined from the magnetic charge density  $\rho_m$  given by  $\rho_m = \nabla \cdot \mathbf{M}(x, y, z)$  (Ref. 32) where the divergence is evaluated numerically based on the OOMMF cell magnetizations. The collection of magnetic charges associated with each cell

$q_m = \rho_m V_C$ , and the resulting field [Eq. (A1)] yields the net field from the domain wall. This method is advantageous in that  $\rho_m$  only arises where  $\nabla \cdot \mathbf{M}(x, y, z)$  is nonzero (i.e. at the domain wall), thereby rendering this approach computationally far less intensive than summation of the fields from each dipole.

\*gvieira@mps.ohio-state.edu

<sup>1</sup>J. M. Perez, L. Josephson, T. O’Loughlin, D. Hogemann, and R. Weissleder, *Nat. Biotechnol.* **20**, 816 (2002).

<sup>2</sup>H. Zeng, J. Li, J. P. Liu, Z. L. Wang, and S. Sun, *Nature* **420**, 395 (2002).

<sup>3</sup>T. J. Yoon, W. Lee, Y. S. Oh, and J. K. Lee, *New J. Chem.* **27**, 227 (2003).

<sup>4</sup>P. S. Doyle, J. Bibette, A. Bancaud, and J. L. Viovy, *Science* **295**, 2237 (2002).

<sup>5</sup>D. Wang, J. He, N. Rosenzweig, and Z. Rosenzweig, *Nano Lett.* **4**, 409 (2004).

<sup>6</sup>T. Mirzabekov, H. Kontos, M. Farzan, W. Marasco, and J. Sodroski, *Nat. Biotechnol.* **18**, 649 (2000).

<sup>7</sup>E. X. Wu, H. Tang, K. K. Wong, and J. Wang, *J. Magn. Reson. Imaging* **19**, 50 (2004).

<sup>8</sup>L. E. Helseth, T. M. Fischer, and T. H. Johansen, *Phys. Rev. E* **67**, 042401 (2003).

<sup>9</sup>M. Donolato, P. Vavassori, M. Gobbi, M. Deryabina, M. F. Hansen, V. Metlushko, B. Ilic, M. Cantoni, D. Petti, S. Brivio, and R. Bertacco, *Adv. Mater.* **22**, 2706 (2010).

<sup>10</sup>L. E. Helseth, T. M. Fischer, and T. H. Johansen, *Phys. Rev. Lett.* **91**, 208302 (2003).

<sup>11</sup>P. Tierno, S. V. Reddy, J. Yuan, T. H. Johansen, and T. M. Fischer, *J. Phys. Chem. B* **111**, 13479 (2007).

<sup>12</sup>P. Vavassori, V. Metlushko, B. Ilic, M. Gobbi, M. Donolato, M. Cantoni, and R. Bertacco, *Appl. Phys. Lett.* **93**, 203502 (2008).

<sup>13</sup>M. Donolato, M. Gobbi, P. Vavassori, M. Leone, M. Cantoni, V. Metlushko, B. Ilic, M. Zhang, S. X. Wang, and R. Bertacco, *Nanotechnology* **20**, 385501 (2009).

<sup>14</sup>M. T. Bryan, J. Dean, T. Schrefl, F. E. Thompson, J. Haycock, and D. A. Allwood, *Appl. Phys. Lett.* **96**, 192503 (2010).

<sup>15</sup>B. B. Yellen, O. Hovorka, and G. Friedman, *Proc. Natl. Acad. Sci. USA* **102**, 8860 (2005).

<sup>16</sup>K. Gunnarsson, P. E. Roy, S. Felton, J. Pihl, P. Svedlindh, S. Berner, H. Lidbaum, and S. Oscarsson, *Adv. Mater.* **17**, 1730 (2005).

<sup>17</sup>R. S. Conroy, G. Zabow, J. Moreland, and A. P. Koretsky, *Appl. Phys. Lett.* **93**, 203901 (2008).

<sup>18</sup>B. B. Yellen, R. M. Erb, H. S. Son, J. Hewlin, H. Shang, and G. U. Lee, *Lab Chip* **7**, 1681 (2007).

<sup>19</sup>T. Henighan, A. Chen, G. Vieira, A. J. Hauser, F. Y. Yang, J. J. Chalmers, and R. Sooryakumar, *Biophys. J.* **98**, 412 (2010).

<sup>20</sup>M. Donolato, A. Torti, N. Kostesha, M. Deryabina, E. Sogne, P. Vavassori, M. F. Hansen, and R. Bertacco, *Lab Chip* **11**, 2976 (2011).

<sup>21</sup>M. T. Bryan, K. H. Smith, M. E. Real, M. A. Bashir, P. W. Fry, P. Fischer, Mi-Young Im, T. Schrefl, D. A. Allwood, and J. W. Haycock, *IEEE Magn. Lett.* **1**, 1500104 (2010).

<sup>22</sup>G. Vieira, T. Henighan, A. Chen, A. J. Hauser, F. Y. Yang, J. J. Chalmers, and R. Sooryakumar, *Phys. Rev. Lett.* **103**, 128101 (2009).

<sup>23</sup>A. Chen, G. Vieira, T. Henighan, M. Howdysshell, J. A. North, A. J. Hauser, F. Y. Yang, M. G. Poirier, C. Jayaprakash, and R. Sooryakumar, *Phys. Rev. Lett.* **107**, 087206 (2011).

<sup>24</sup>G. Ruan, G. Vieira, T. Henighan, A. Chen, D. Thakur, R. Sooryakumar, and J. O. Winter, *Nano Lett.* **10**, 2220 (2010).

<sup>25</sup>T. Taniyama, I. Nakatani, T. Namikawa, and Y. Yamazaki, *Phys. Rev. Lett.* **82**, 2780 (1999).

<sup>26</sup>M. J. Donahue and D. G. Porter, Interagency Report NISTIR 6376, National Institute of Standards and Technology, Gaithersburg, MD, 1999.

<sup>27</sup>See Supplemental Material at <http://link.aps.org/supplemental/10.1103/PhysRevB.85.174440> for bead manipulation videos.

<sup>28</sup>U. Häfeli, W. Schütt, J. Teller, and M. Zborowski, *Scientific and Clinical Applications of Magnetic Carriers* (Plenum Press, New York, 1997).

<sup>29</sup>S. Smith, L. Finzi, and C. Bustamante, *Science* **258**, 1122 (1992).

<sup>30</sup>J. P. Rickgauer, D. N. Fuller, and D. E. Smith, *Biophys. J.* **91**, 4253 (2006).

<sup>31</sup>A. Hubert and R. Schäfer, *Magnetic Domains: The Analysis of Magnetic Microstructures* (Springer, Berlin, 1998).

<sup>32</sup>J. D. Jackson, *Classical Electrodynamics*, 3rd ed. (Wiley, Hoboken, NJ, 1999).